MECHANISM OF DUCTILE FRACTURE OF THE LOW CARBON CAST STEEL

M.U. Biel*

The influence of stress state on the effective plastic strain and maximum tensile stress required to initiate fracture in low carbon cast steel was investigated. A criterion for ductile failure, where a critical fracture stress is locally exceeded over some characteristic distance ahead of the crack tip, is proposed. The process zone size for ductile fracture, using the tensile fracture stress and critical effective strain criterion has been evaluated. An attempt was made to identify the effective inclusion size governing the microfracture process.

INTRODUCTION

Much research work has been carried out (in the last decade) to get a better understanding of the mechanism of crack initiation at microscopic level. Considerable work has concentrated on predicting the fracture toughness of brittle alloys. However, ductile fracture has not been investigated so extensively and many problems remain unresolved. The fracture processes in notched structures takes place in a small volume of material in the vicinity of the notch and is influenced by the microstructural parameters such as inclusion distribution, matrix structure as well as the stress and strain distribution ahead of the crack tip. To understand the relation of the fracture toughness to the microstructure a critical parameter which characterizes the local fracture process should be determined.

Little is known about the ductile fracture of cast alloys; therefore this paper is concerned with the investigation of the micromechanisms of fracture in a low carbon cast steel.

* Foundry Research Institute, Cracow, Poland

The object of this study is to determine the criterion for ductile crack initiation. This local criterion has been related to the microstructure and to the macroscopic fracture toughness. The importance of the triaxiality factor, the inclusions and the second phase particles on crack initiation have been thoroughly investigated.

To realize the main objects of this paper comprehensive investigations have been carried out including:

- determination of mechanical properties (yield stress, ultimate tensile stress, elongation and hardening exponent),
- fracture toughness determination using the δ_c and J_{Ic} method,
- the critical fracture stresses and effective plastic strain related to the stress state evaluation,
- statistical size distribution of inclusions
- quantitative fractography of specimens broken under different degrees of plane stress
  process zone size evaluation using the critical stress condition and the HRR solution and using the critical effective strain condition and Rice-Johnson's solution.

MATERIAL

A low carbon cast steel with a manganese addition was used. The chemical composition is given in table 1.

TABLE 1 - Composition of tested Cast Steel in Weight Percent.

C	Si	Mn	S	P
0,18	0,52	1,06	0,018	0,016

The material was prepared by normalising at 1183 K for 4 h followed by air cooling.

TENSILE AND FRACTURE TOUGHNESS TESTS

The standard round tensile specimens were tested on a 250 kN Instron machine to determine the tensile properties. SEN three point bending specimens of 15x30x150 mm were used for fracture toughness determination. The material exhibits high toughness so that the thickness condition for valid fracture toughness K_{Ic} data could not be satisfied. Therefore the COD and J-integral methods for toughness evaluation were used simultaneously. The critical crack tip opening displacement was determined according to the BS 5762: 1979. The three point bending samples were used to determine

critical J-integral evaluation according to Japanese Standard ISME Standard S 001-1981. To detect crack initiation the electro-potential drop technique was used.

Moreover the α_o coefficient and the hardening exponent n appearing in the Ramberg-Osgood equation were determined. Mechanical properties and fracture test data were determined at room temperature. The results of these tests are given in tables 2 and 3, respectively.

TABLE 2 - Mechanical Properties of tested Cast Steel.

σ_y	UTS	A_5	z	$\varepsilon = \ln \frac{1}{1-z}$	n	α_o
[MPa]	[MPa]	[%]	[%]			
282.1	504.2	-36.0	64.6	1.03	4.75	5.75

TABLE 3 - Fracture Data.

δ_c	J_{Ic}	K_{Ic}	B_{min}	$m = \frac{J_{Ic}}{\delta \sigma_y}$
[mm]	[kJ/mm²]	[MPa $\sqrt{m}$]	[mm]	
0.400	212.7	221.6	13.5	1.87

INFLUENCE OF THE STRESS STATE ON DUCTILE FAILURE INITIATION

To explain the process of ductile fracture in a triaxial stress field some critical parameters of ductile fracture initiation have been proposed. There are several conditions suggested as critical for ductile crack initiation: critical strain by Krafft (1), critical effective strain by McKenzie et al. (2) and critical equivalent stress by Mutoh (3). However sufficient results have not been obtained yet, mainly because none of the relevant critical conditions above reflect the physical processes occuring during ductile crack initiation. Therefore it appeared useful trying to determine the critical conditions causing the crack initiation in the material under test. In describing the failure process in the vicinity of the crack tip, it was assumed that the critical parameter is independent of the triaxiality of the stress state defined as $\sigma_m/\bar{\sigma}$.

This assumption was made because the triaxiality factor changes from 0.58 at the blunting of the crack tip to 2.4 at a distance of 1.96. Experiments were made on circumferentially notched round tension specimens. The samples are shown in figure 1. The different degrees of triaxiality of stress states were obtained by varying the notch radius. Five different notch radii were used and thus five different values of stress triaxiality factors were obtained. These were 0.39, 0.49c, 0.73, 1.10 and 1.34.

To determine the stress distribution at the minimum cross-section the Bridgeman (4) analysis was applied. The tests were interrupted at the point of failure initiation as defined in reference (2). At this moment initiation took place by the coalescence of voids at large inclusions. The axial stress σ_{zz}, equivalent stress $\bar{\sigma}$, mean stress σ_m and stress at the matrix-second phase particle boundary σ^A_{rr} calculated according to Argon et al. (5), as well as the effective plastic strain ε_p at this point, were compared to the critical fracture stress for cleavage. These fracture data are given in table 4 and shown in figure 2. The experimental determination of critical fracture stress σ_c for cleavage fracture was made by Griffith and Owen's (6) method. This fracture stress was found to be σ_c = 1416 MPa.

TABLE 4 - Fracture under Different Degrees of Plane Stress.

$\sigma_m/\bar{\sigma}$		$\bar{\varepsilon}_c$	$\bar{\sigma}_c$	σ_{zz}	σ_m	σ^A_{rr}
original	at crack initiation		[MPa]	[MPa]	[MPa]	[MPa]
0.33	0.38	1.05	1054	1145	400	1454
0.49	0.45	0.65	1079	1208	485	1565
0.73	0.53	0.45	921	1108	488	1409
1.10	0.73	0.36	918	1282	670	1588
1.34	0.91	0.24	770	1212	701	1471

METALLOGRAPHIC INVESTIGATIONS

The inclusion size distribution was studied using quantitative microscopic techniques by means of a Cambridge Stereoscan 720. The inclusion sizes were grouped into eight classes. The mean of the nearest neighbour distance (for each class was calculated) as well as the ratio of the nearest neighbour distance to the mean inclusion diameter $\bar{D}$. The results are given in table 5.

The fracture surfaces of both the tensile and SEN specimens were studied by means of a Cambridge Instruments Stereoscan 170 SEM. Fracture by void coalescence was observed in all specimens. For the round notched tensile specimen the relationship between the stress triaxiality factor and dimple size on the fracture surface was investigated. A quantitative analysis was made in which the number of dimples per square mm $\bar{S}_D$, the mean distance between centres of dimples ℓ_D and mean dimple size $\bar{D}_D$ were determined for samples with initial triaxiality factors of 0.49 and 1.1. The results are given in table 4. The fracture surfaces are shown in figure 3 and figure 4.

TABLE 5 - Inclusion Size Distribution.

number of class	D_{min} [μm]	D_{max} [μm]	D_{mean} [μm]	N_V [mm^{-3}]	ℓ_o [μm]	$\ell_{o/D_{mean}}$
1	0	1.43	0.715	430085	7.3	10.20
2	1.43	2.86	2.14	239793	8.9	4.16
3	2.86	4.30	3.58	830368	12.8	3.57
4	4.30	5.73	5.01	16476	21.8	4.35
5	5.73	7.16	6.44	5379	31.6	4.90
6	7.16	8.60	7.88	3957	35.0	4.40
7	8.60	10.00	9.30	431	73.3	7.88
8	10.00	11.40	10.70	1417	49.3	4.60

TABLE 6 - Dimple Distribution as a Function of the Stress Triaxiality Factor.

$\sigma_m/\bar{\sigma}$ original	$\sigma_m/\bar{\sigma}$ at crack initiation	number of dimples per square mm [mm^{-2}]	$\bar{D}$ [μm]	$\bar{\ell}_D$ [μm]	$\bar{D}_2/\bar{D}_1$
0.49	0.45	6180	14.4	12.7	1.27
1.10	0.73	3796	18.3	16.2	

DISCUSSION OF THE RESULTS

The results of J_{Ic} and δ_c measurements were compared and a relationship $J_{Ic} = 1.87\ \sigma_y\ \delta_c$ was obtained. This relationship is liable to further discussion because the HRR analysis of Hutchinson (7) and that of Rice and Rosengreen (8) is expressed in terms of J, while Rice and Johnson's (9) solution is given in terms of δ.

To estimate the process zone size (PZS) ℓ_c^* the critical value of the parameter, which characterizes the fracture conditions should be determined. It is assumed that this parameter should be not dependent on the stress triaxiality factor. As can be seen in figure 2 the maximum axial stress σ_{zz} and the stress at the matrix-second phase particle boundary σ_{rr}^A at fracture are insensitive to the stress system triaxiality. This is not the case for the calculated critial cleavage fracture stress σ_c. Therefore σ_{zz} at fracture was taken as the critical parameter controlling the ductile fracture stress σ_c^*. This is the assumption made in the model developed by Ritchie et al (10). It is also in agreement with Ludwik Schen's (11) suggestion that failure will occur when the maximum principal stress reaches a critical value, which does not depend greatly on the amount of plastic strain.

The PZS was calculated for the critical stress conditions. It was assumed that fracture occurs when the maximum stress exceeds the critical ductile stress over a microstructurally significant distance ℓ_c^* ahead of the crack tip. To determine the stress distribution near the crack tip the HRR small scale yielding solution was used:

$$\sigma_{ij} = \sigma_y \left(\frac{J}{\alpha_o \cdot \sigma_y \cdot \varepsilon_o \cdot I_n \cdot \ell_c^*} \right)^{\frac{1}{n+1}} \cdot \tilde{\sigma}_{ij}(\theta.n) \qquad (1)$$

Substituting σ_c^* and J_{Ic} into J the process zone size was obtained. The size of process zone computed from this equation using experimental J_{Ic} and σ_c^* data was equal to $\ell_c^* = 504\ \mu m$. This result is compared to the PZS calculated using the critical effective strain criterion. According to this criterion. ductile fracture takes place if a critical effective strain is locally exceeded in the process zone ahead of the crack tip. However the critical effective strain is a strong function of the stress triaxiality which itself varies with distance from the crack tip. To estimate the

PZS a relationship was obtained by eliminating x_o/σ from the $\bar{\varepsilon}$ vs. x_o/σ and the $\sigma_m/\bar{\sigma}$ vs. x_o/σ relations in reference (9). These are shown in graphical form in figure 5 following McKanzie et al.(2). Thus the curve in figure 6 was obtained. Each point on these trajectories corresponds to a value x_o/σ, which can be deduced by returning to the original data. Curve 2 is compared to the failure locus $\sigma_m/\bar{\sigma}$ vs. $\bar{\varepsilon}$, determined experimentally curve 1 in figure 6. The intersection point at $\sigma_m/\bar{\sigma} = 1.36$ defines the distance ahead of the crack tip where the critical effective strain is exceeded. Returning to figure 5 a ratio $x_o = 1.2$ can be obtained. Taking $\delta_c = 0{,}400$ mm a PZS of 480 µm is obtained for the two conditions being quite similar.

To identify the most effective inclusion for nucleating a void it was assumed that the mean space between them $\bar{\ell}_o$ should be equal to the mean distance between the centres of the dimples $\bar{\ell}_D$.

Therefore the mean dimple spacings $\bar{\ell}_D$ (table 6) were compared to the inclusion size distribution (table 5). It was found that $\bar{\ell}_D$ is equal to the inclusion spacing in class 3 and these inclusions were therefore assumed to be the most effective ones for ductile crack initiation. For this class the ratio of the mean distance $\bar{\ell}_o$ to the inclusion diameter is also smallest. This result is in agreement with the theoretical solution given by McClintock (12) and the experimental observations of Kumar and Pandey (13). One can try to relate the PZS to some of the microstructural features. To this end, the grain size d = 17,2 µm and the prior austenitic grain size $d_A = 19{,}3$ µm was determined. It can be seen that the size PZS is of the order of 25 ÷ 30 times the grain size or of 40 times the most effective inclusion spacing. It is interesting to note that for the material tested the stress at the matrix-second phase particles boundary σ^A_{rr} is independent of the stress triaxiality factor (figure 2). Moreover the obtained value of $\sigma^A_{rr} = 1496$ MPa is not very different from the critical stress at the boundary between the cementite particles and ferritic matrix $\sigma^A_{rr} = 1650$ MPa given by Argon and Im (14). Fractographic studies of the fracture surface reveal that the instability fracture between voids and the

crack tip and between neighbouring voids occurs by fine-scale coalescence of microvoids.

CONCLUSION

The above study dealt with a simple ductile fracture model for predicting the crack initiation process under critical stress conditions. The fracture process takes place if a stress of 1200 MPa is exceeded over a distance of 500 µm ahead of the crack tip. The critical ductile fracture stress depends indirectly on the voids initiated at inclusions and microcracks at carbide/matrix boundary.

The critical ductile fracture stress is independent of the stress triaxiality factor. On the base of stereographic, and fractographic investigations it could be suggested, that the most effective inclusion distribution for initiating the microfracture process is the one, where the ratio of the inclusion spacing to the inclusion size is minimum. The PZS was observed to extend over a number of dimples.

SYMBOLS USED

α_o = Ramberg Osgood equation coefficient

n = hardening exponent

A_s = elongation (%)

z = reduction in area (%)

σ_{zz} = axial stress (MPa

$\bar{\sigma}$ = equivalent stress (MPa)

σ_m = mean stress (MPa)

σ_y yield stress (MPa)

$\bar{\varepsilon}$ = effective plastic strain

d_o = original diameter in the notched cross-section

σ_{rr}^{A} = stress at matrix second phase particle interface (MPa)

D = inclusion diameter (µm)

N_v = inclusion number in volume unit (mm^{-3})

ℓ_o = nearest neighbour spacing (µm)

D_D = dimple diameter (µm)

ℓ_D = first neighbour spacing of dimples (µm)

S_D = number of dimples per square (mm)

σ_c = critical cleavage fracture stress (MPa)

ε_o = strain at yield stress

ℓ_c^* = process zone size (μm)

J_n = constant depending on stress state and hardening exponent

$\bar{\sigma}_{ij}$ = constant depending on stress state and hardening exponent

σ_c^* = critical ductile fracture stress (MPa)

REFERENCES

(1) Krafft, J.M., Appl. Mat. Res., Vol. 3, 1984, pp. 88-101.

(2) McKenzie, A.C., Hancock, J.W. and Brown, D.K., Eng. Fract. Mech., Vol. 9, 1977, pp. 167-188.

(3) Mutoch, Y., Eng. Fract. Mech., Vol. 17, 1983, pp. 219-226.

(4) Bridgeman, P.W., Studies in Large Flow and Fracture, McGraw-Hill, New York, USA, 1952.

(5) Argon, A.S., Im J. and Safoglu R., Met. Trans. Vol. 64A, 1975, pp. 825-837.

(6) Griffith, J.E. and Owen, D.R., J. Mech. Phys. Solids, Vol. 19, 1971, pp. 419-431.

(7) Hutchinson, J.W., J. Mech. Phys. Solids, Vol. 16, 1968, pp. 13-31.

(8) Rice, J.R. and Rosengreen, G.T., J. Mech. Phys. Solids, Vol. 16, 1968, pp. 1-12.

(9) Rice, J.R. and Johnson, A.A., Inelastic Behaviour of Solids. Edited by Kaninen, M.F., McGraw-Hill, New York, A.S.A., 1969.

(10) Ritchie, R.O., Knott, J.F. and Rice, J.R., J. Mech. Phys. Solids, Vol. 21, 1973, pp. 395-410.

(11) Ludwik, P., Schen, R., Stahl und Eisen, Vol. 43, 1923, pp. 999-1001.

(12) McClintock, F.A., J. Appl. Mech. Vol. 35, 1968, pp. 363-375.

(13) Kumar, A.N. and Pandey, R.K., Eng. Fract. Mech., Vol. 19, 1984, pp. 239-249.

(14) Argon, A.S., Im J. Met. Trans., Vol. 6A, 1975, pp. 839-851.

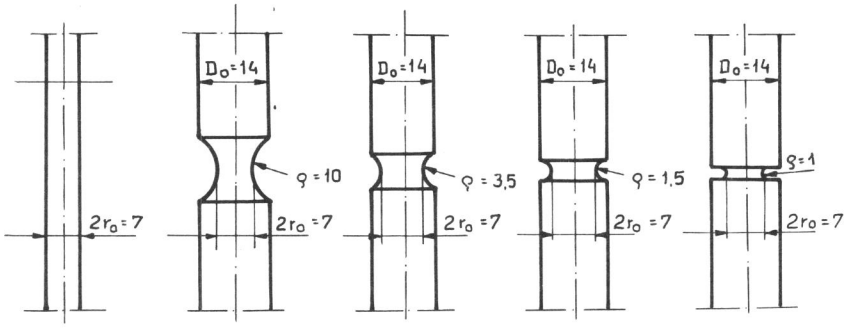

Figure 1 Circumferential notched round tensile specimens

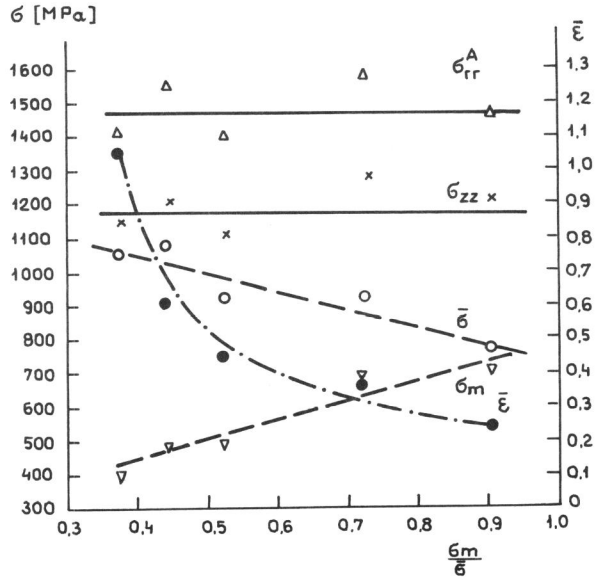

Figure 2 Fracture data under different stress state conditions

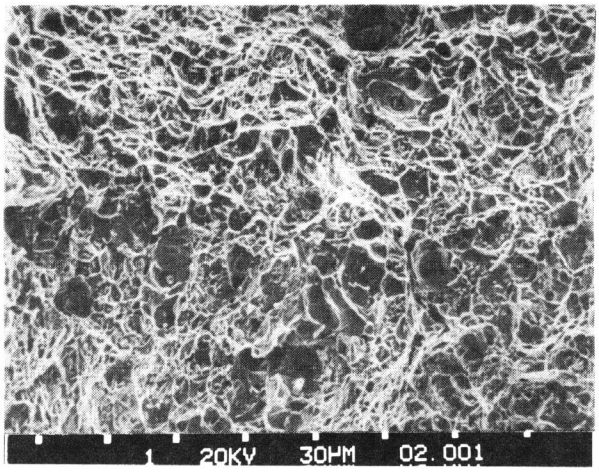

Figure 3 Ductile fracture surface $\sigma_m/\bar{\sigma} = 0.49$

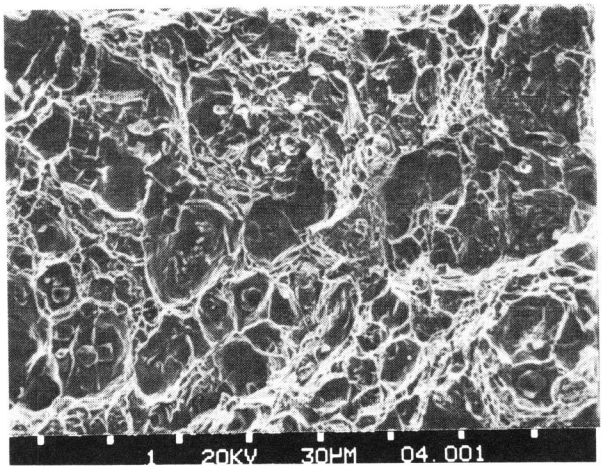

Figure 4 Ductile fracture surface $\sigma_m/\bar{\sigma} = 1.10$

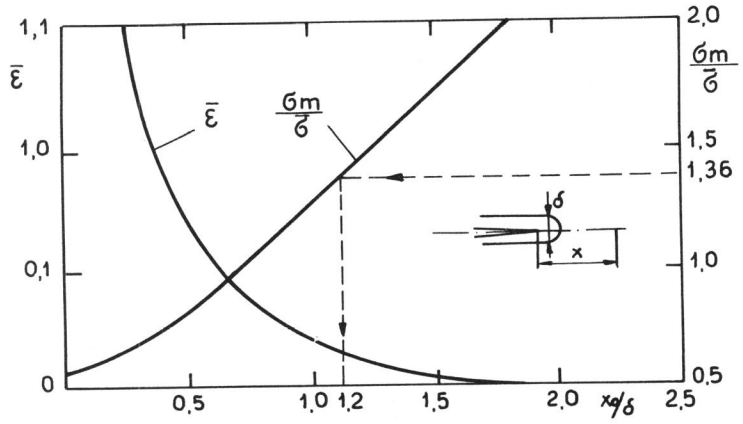

Figure 5 Distribution effective strain and stress triaxiality near crack tip after Rice and Johnson (9)

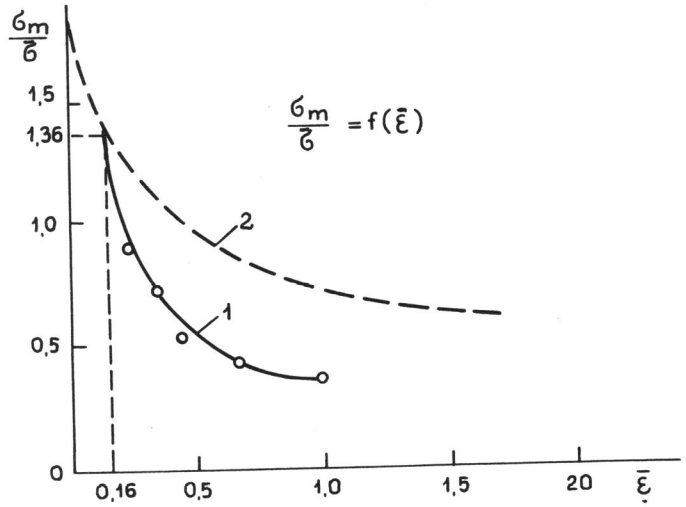

Figure 6 $\sigma_m/\bar{\sigma}$ vs. $\bar{\varepsilon}$: curve 1 - experimentally determined
curve 2 - from Rice-Johnson solution